

Water Absorption from Gas Very Near the Massive Protostar AFGL 2136 IRS 1*

Nick Indriolo¹, D. A. Neufeld¹, A. Seifahrt², M. J. Richter³

ABSTRACT

We present ground-based observations of the ν_1 and ν_3 fundamental bands of H₂O toward the massive protostar AFGL 2136 IRS 1, identifying absorption features due to 47 different ro-vibrational transitions between 2.468 μm and 2.561 μm . Analysis of these features indicates the absorption arises in warm ($T = 506 \pm 25$ K), very dense ($n(\text{H}_2) > 5 \times 10^9 \text{ cm}^{-3}$) gas, suggesting an origin close to the central protostar. The total column density of warm water is estimated to be $N(\text{H}_2\text{O}) = (1.02 \pm 0.02) \times 10^{19} \text{ cm}^{-2}$, giving a relative abundance of $N(\text{H}_2\text{O})/N(\text{H}_2) \approx 10^{-4}$. Our study represents the first extensive use of water vapor absorption lines in the near infrared, and demonstrates the utility of such observations in deriving physical parameters.

Subject headings: astrochemistry — ISM: molecules

1. INTRODUCTION

Water is expected to be one of the most abundant species in warm, dense regions of the interstellar medium where its formation is facilitated by neutral-neutral reactions. In the innermost regions of protostellar envelopes, chemical models predict that nearly half of the total oxygen abundance is in the form of gas-phase H₂O, $n(\text{H}_2\text{O})/n(\text{H}_2) \approx 10^{-4}$, while the other half is in CO (Ceccarelli et al. 1996). Because the relative populations in excited rotational states of H₂O are highly dependent on physical parameters (e.g., temperature,

¹Department of Physics and Astronomy, Johns Hopkins University, Baltimore, MD 21218

²Department of Astronomy and Astrophysics, University of Chicago, Chicago, IL 60637

³Department of Physics, University of California Davis, Davis, CA 95616

*Based on observations collected at the European Organisation for Astronomical Research in the Southern Hemisphere, Chile as part of program 089.C-0321

density, radiation field), water can be a powerful diagnostic of the conditions in protostellar environments.

Due to abundant water in Earth’s atmosphere, ground-based observations of astrophysical water vapor have been rather limited in scope, primarily focusing on maser emission. Indeed, the first detection of interstellar water was made by observing maser emission from the $6_{1,6}-5_{2,3}$ transition of H_2O near 22 GHz (Cheung et al. 1969). Since then, ground-based observations of water masers in star forming regions have expanded to include the following transitions: $10_{2,9}-9_{3,6}$ at 321 GHz (Menten et al. 1990a); $5_{1,5}-4_{2,2}$ at 325 GHz (Menten et al. 1990b); $3_{1,3}-2_{2,0}$ at 183 GHz (Cernicharo et al. 1990); $6_{4,3}-5_{5,0}$ at 439 GHz (Melnick et al. 1993); $6_{4,2}-5_{5,1}$ at 471 GHz (Melnick et al. 1993). Of the various water maser transitions, that at 22 GHz is by far the most frequently observed, with detections in over 1000 different sources (Benson & Little-Marenin 1996; Valdetaro et al. 2001; Sunada et al. 2007). These H_2O masers are good tracers of high-mass star formation, likely arising in dense, shocked gas associated with molecular outflows.

Ground-based observations of water in non-maser transitions are extremely limited, with only a few studies detecting emission in protoplanetary disks from transitions in the near-IR (Najita et al. 2000; Carr et al. 2004; Salyk et al. 2008) and mid-IR (Pontoppidan et al. 2010a). Instead, observations of astrophysical water in non-maser transitions have relied mostly on space-based observatories. ISO-SWS (Infrared Space Observatory-Short Wavelength Spectrometer) revealed water absorption near $6 \mu\text{m}$ from the ν_2 ro-vibrational band toward massive protostars (Boonman & van Dishoeck 2003). *Spitzer*-IRS (InfraRed Spectrometer) observations showed H_2O emission in pure rotational transitions across the mid-infrared in protoplanetary disks (e.g., Pontoppidan et al. 2010b). Most recently, *Herschel*-HIFI (Heterodyne Instrument for the Far-Infrared) has enabled observations of water in several of the lowest rotational states, including the ground state (e.g., van Dishoeck et al. 2011; Sonnentrucker et al. 2010). Unfortunately, the current lack of space-based observatories capable of observing water threatens to stagnate our investigations of astrophysical H_2O unless new methods are devised. Here, we present the first extensive study of the $v = 1-0$, ν_1 and ν_3 bands of water—detected in absorption toward AFGL 2136 IRS 1 via ground-based observations in the near-IR while targeting the $v = 1-0$, $R(0)$ transition of HF at $2.499385 \mu\text{m}$ (Indriolo et al. 2013)—and examine the potential of such observations for future studies.

2. TARGET CHARACTERISTICS

AFGL 2136 is a star-forming region at a distance of about 2 kpc that shows a complex morphology at near infrared (H -band and K -band) wavelengths due to dust grains reflecting light from the central source, IRS 1, an embedded massive protostar with luminosity $L \sim 5 \times 10^4 L_{\odot}$ (Minchin et al. 1991; Kastner et al. 1992; Murakawa et al. 2008). Polarization measurements are indicative of a circumstellar disk at a position angle of about 45° (Kastner et al. 1992; Murakawa et al. 2008), and emission maps in CO show massive molecular outflows oriented perpendicular to the proposed disk (Kastner et al. 1994). Gas velocities in the outflow lobes suggest a modest—less than 40° —inclination with respect to the plane of the sky. A hypothetical picture of AFGL 2136 IRS 1 based on mid-infrared interferometry shows an envelope, torus, and disk component (de Wit et al. 2011).

Infrared spectra reveal both warm and cold gas along this line of sight. Absorption due to gas-phase CO (Mitchell et al. 1990) and H₂O (Boonman & van Dishoeck 2003) in highly excited states is observed, along with ice bands of H₂O, CO₂, and CH₃OH (Willner et al. 1982; van Dishoeck et al. 1996; Brooke et al. 1999; Gerakines et al. 1999). The warm gas is thought to be in the core surrounding the massive protostar, while the cold gas is in the outer envelope or molecular cloud from which the protostar collapsed. Observations of CO, CS, and H₂CO in emission give a systemic velocity of $v_{\text{LSR}} = 22.8 \text{ km s}^{-1}$ for the molecular cloud (van der Tak et al. 2000). A small (3–5 km s⁻¹) redshift with respect to the systemic velocity distinguishes the warm gas from the cold cloud.

3. OBSERVATIONS & DATA REDUCTION

AFGL 2136 IRS 1 was observed on July 6, 2012 for a total of 3960 s using the Cryogenic High-resolution Infrared Echelle Spectrograph (CRIRES; Käufel et al. 2004) on UT1 at the Very Large Telescope. Observations were performed in service mode, and CRIRES was used with its 0".2 slit to provide a resolving power (resolution) of about 100,000 (3 km s⁻¹). A reference wavelength of 2502.8 nm set the wavelength ranges on detectors 1 through 4 to be 2.4679–2.4796 μm , 2.4831–2.4943 μm , 2.4974–2.5081 μm , and 2.5111–2.5212 μm , respectively. Due to the lack of a bright natural guide star, the adaptive optics system was not utilized. The slit was oriented at a position angle of 45° (i.e., along a northeast-to-southwest axis) to minimize interference from surrounding nebulosity. Spectra were obtained in an ABBA pattern with 10" between the two nod positions and $\pm 3''$ jitter width. Details regarding the data reduction procedure can be found in Indriolo et al. (2013). Processed one-dimensional science spectra were divided by model atmospheric spectra (Seifahrt et al. 2010) for the purpose of removing atmospheric absorption lines. Science spectra, model

atmospheric spectra, and the resulting ratioed spectra in select wavelength regions are shown in Figure 1.

4. RESULTS & ANALYSIS

In the full wavelength range covered by our observations we identified 35 separate absorption features arising from 47 different transitions of the $v = 1-0 \nu_1$ (symmetric stretch), $v = 1-0 \nu_3$ (asymmetric stretch), and $v = 2-0 \nu_2$ (bend) bands of H_2O . All of these are shown in Figure 2 in velocity space, along with Gaussian fits to the absorption features. Fits are comprised of either one or two Gaussian components, with two components used in cases where there are multiple features (e.g., panels D1 & E3), or the main feature has a prominent “shoulder” on the right-hand side (e.g., panels B5 & F2). Parameters extracted from the fitting procedure—LSR velocity, velocity FWHM, equivalent width—are given in Table 1, along with transition labels, column densities, and a key denoting which transitions are shown in each panel in Figure 2. The mean LSR velocity is $24.6 \pm 1.1 \text{ km s}^{-1}$, and the mean velocity FWHM is $13.6 \pm 2.5 \text{ km s}^{-1}$. A rotation diagram (Figure 3) was made using column densities reported in Table 1. The relatively straight line traced out by the data in $\ln(N/g)$ versus lower state energy (where g is the statistical weight) is indicative of gas with a single temperature in local thermodynamic equilibrium (LTE).

To determine the physical conditions in the absorbing gas, we have modeled the excitation of the lowest 120 rotational states of ortho- and para-water using a statistical equilibrium code to determine the expected level populations. In this analysis, we used an escape probability method to treat the effects of radiative trapping. For the collisional excitation of H_2O by H_2 , we adopted the rate coefficients computed recently by Daniel et al. (2011), and then used an artificial neural network method (Neufeld 2010) to extrapolate these to states of higher energy than those for which calculations were available. We also included the effects of radiative pumping—in both pure rotational and ro-vibrational transitions—by the infrared continuum radiation emitted by AFGL 2136 IRS 1; here, we adopted the spectral energy distribution for AFGL 2136 IRS 1 implied by a fit to available data obtained by Murakawa et al. (2008, the TO model plotted in their Figure 7).

The importance of radiative excitation depends upon the assumed distance, d , of the absorbing material from the source of continuum radiation. For $d > 200 \text{ AU}$, radiative excitation has a negligible effect upon the population of the rotational states that we have observed; in this limit, the observed level populations place strong constraints upon the temperature, H_2 density, and total water column density. A chi-squared minimization yields a best-fit gas temperature of $506 \pm 25 \text{ K}$, a best-fit H_2O column density of $(1.02 \pm 0.02) \times$

10^{19} cm^{-2} , and places a 3σ lower limit of $5 \times 10^9 \text{ cm}^{-3}$ on the H_2 density.⁴ In Figure 4, we show the contours of chi-squared in the temperature-density plane, obtained in the limit $d > 200 \text{ AU}$. For $d < 200 \text{ AU}$, the effects of radiative pumping reduce our lower limit on the H_2 density by up to an order of magnitude, the weakest constraints being obtained for $d \sim 120 \text{ AU}$.

Taking the range of warm H_2 column densities previously determined ($N(\text{H}_2) = (5.5\text{--}9.8) \times 10^{22} \text{ cm}^{-2}$; Indriolo et al. 2013), we find a relative abundance of $N(\text{H}_2\text{O})/N(\text{H}_2) = (1.0\text{--}1.9) \times 10^{-4}$, in relatively good agreement with predictions made by chemical models for warm, dense gas near massive protostars (e.g., Ceccarelli et al. 1996; Doty et al. 2002). The lower limit on the number density can be used with the total H_2 column density to estimate the size of the region where the H_2O absorption occurs. Adopting the larger value of $N(\text{H}_2) = 9.8 \times 10^{22} \text{ cm}^{-2}$, the density limit of $n(\text{H}_2) > 5 \times 10^9 \text{ cm}^{-3}$ results in a path-length limit of $L < 2 \times 10^{13} \text{ cm}$ (1.3 AU). The weaker density constraints in the scenario where radiative pumping is important relax this size limit to $L \lesssim 13 \text{ AU}$. Given the high density, high temperature, and small path length, this gas must be located fairly close to the central protostar, likely in the inner envelope or a circumstellar disk.

5. DISCUSSION

5.1. Comparison with Observational Results

The physical parameters derived from our analysis can be compared to those found by previous studies of AFGL 2136 IRS 1. Water absorption has been observed in this source before via the $v = 1\text{--}0 \nu_2$ band near $6 \mu\text{m}$ using ISO-SWS (van Dishoeck & Helmich 1996; Boonman & van Dishoeck 2003). The lower spectral resolution of that instrument ($\lambda/\Delta\lambda \sim 1400$) made it so that all absorption features were blends of several different transitions. In order to determine best-fit parameters, Boonman & van Dishoeck (2003) produced a suite of synthetic spectra arising from different combinations of T , $N(\text{H}_2\text{O})$, and b (Doppler line width), and compared them to the observed spectrum. Adopting a value of $b = 5 \text{ km s}^{-1}$, they found $T = 500_{-150}^{+250}$ and $N(\text{H}_2\text{O}) = (1.5 \pm 0.6) \times 10^{18} \text{ cm}^{-2}$. The excitation temperature is in excellent agreement with our findings, but their water column density is about 7 times smaller. This result was obtained with a model only considering absorption, and Boonman & van Dishoeck (2003) postulated that emission filling in some of

⁴Note that $N(\text{H}_2\text{O})$ is dependent on the single temperature model utilized and is likely not as tightly constrained as the quoted uncertainties suggest.

the absorption features could result in column densities being underestimated by factors of 3–6.

It is unclear to what extent emission competes with absorption in the H₂O spectra presented by Boonman & van Dishoeck (2003). If a spherical cloud lies entirely within the telescope beam (slit), then every absorbed photon should be balanced by an emitted photon. Because $\Delta J = +1$ transitions are favored, *R*-branch lines should appear in absorption while *P*-branch lines appear in emission—a phenomenon observed in the $v = 1-0$, ν_2 band of water toward Orion BN/KL (Gonzalez-Alfonso et al. 1998). However, the high-mass protostars observed by Boonman & van Dishoeck (2003) show neither this signature nor any clear signs of emission at all. Of course, astronomical sources are not idealized spherical objects, and a larger amount of material along the line of sight—e.g., the disk/torus structure of AFGL 2136 IRS 1 described in Section 2—would preferentially show absorption. Additionally, at very high densities collisional de-excitation of vibrationally excited states could compete with spontaneous emission, again favoring absorption being observed. Our own observations reveal no hint of emission in the ν_1 and ν_3 bands (although we only cover *R*-branch lines), and archival TEXES (Texas Echelon Cross Echelle Spectrograph) observations near 8.5 μm show the ν_2 12_{5,8}–13_{6,7} transition—a *P*-branch line—in absorption. For all of these reasons, we neglect the possible effects of emission during the analysis of our data.

An alternative probe of density and temperature is CO. Absorption lines from the $v = 1-0$ and $v = 2-1$ bands of ¹²CO and the $v = 1-0$ band of ¹³CO near 4.7 μm were observed toward AFGL 2136 IRS 1 by Mitchell et al. (1990). Lines in the $v = 1-0$ band of ¹²CO are optically thick, so the ¹³CO band is used in their main analysis. Mitchell et al. (1990) find both a cold ($T = 17_{-3}^{+5}$ K, $N(^{13}\text{CO}) = (1.2 \pm 0.5) \times 10^{17} \text{ cm}^{-2}$) and warm ($T = 580_{-50}^{+60}$ K, $N(^{13}\text{CO}) = (2.5 \pm 0.7) \times 10^{17} \text{ cm}^{-2}$) gas component. The temperature of the warm component is in good agreement with that found by our analysis, and the CO abundance, $N(^{12}\text{CO})/N(\text{H}_2) = (1.8\text{--}3.2) \times 10^{-4}$ assuming ¹²CO/¹³CO = 70 (Sheffer et al. 2007, and references therein), is indicative of the case where nearly all of the carbon and half of the oxygen are in the form of CO, while the remaining oxygen is in H₂O. Additionally, detection of the $v = 2-1$ band of ¹²CO in absorption indicates high density ($n(\text{H}_2) \gtrsim 10^{10} \text{ cm}^{-3}$), as an observable population in the first vibrationally excited state would not otherwise be maintained (Mitchell et al. 1990). This is consistent with the lower limit we have placed on density.

The same set of observations used in our paper also revealed absorption in both the $v = 1-0$, *R*(0) and *R*(1) transitions of HF at 20.3 km s^{−1} and 24.5 km s^{−1}, respectively (Indriolo et al. 2013). Given the relative populations in these levels, the velocity match between the *R*(1) line and the warm H₂O, and the characteristic ~ 4 km s^{−1} shift between

the two lines, we concluded that the $R(0)$ absorption arises in the cold molecular cloud, while the $R(1)$ absorption arises in the same warm gas where we see water. Significant population in the $J = 1$ level requires either radiative pumping or high density, $n(\text{H}_2) \gtrsim 10^9 \text{ cm}^{-3}$ (Neufeld et al. 1997), so the HF results indicate conditions similar to those inferred from H_2O and CO.

Kinematics in the gas surrounding AFGL 2136 IRS 1 are also of interest. As mentioned before, there is a slight shift between the velocity found for warm ^{13}CO ($v_{\text{LSR}} = 26.5 \text{ km s}^{-1}$) and the systemic velocity ($v_{\text{LSR}} = 22.8 \text{ km s}^{-1}$) of the cold cloud surrounding the protostar (Kastner et al. 1994; van der Tak et al. 2000). Kastner et al. (1994) suggested that the difference in velocity may indicate that the warm gas is infalling toward the central protostar. The average velocity found for warm H_2O ($v_{\text{LSR}} = 24.6 \text{ km s}^{-1}$) is about halfway between the cold cloud and warm ^{13}CO velocities, a somewhat puzzling result. Water maser emission at 22.23508 GHz ($6_{1,6} \rightarrow 5_{2,3}$) has been observed toward AFGL 2136 in several instances (Benson & Little-Marenin 1996; Valdetaro et al. 2001; Menten & van der Tak 2004; Sunada et al. 2007), with the peak emission between 26.7 km s^{-1} and 27.5 km s^{-1} . The interferometric observations of Menten & van der Tak (2004) reveal compact maser emission in a region $600 \times 1000 \text{ AU}$ around what they dub radio source 4 (RS4), which is coincident with IRS 1 within positional uncertainties. Conditions necessary to produce this maser emission ($T \sim 400 \text{ K}$, $n(\text{H}_2) \sim 10^9 \text{ cm}^{-3}$; Elitzur et al. 1989) are similar to those that we have inferred, and Menten & van der Tak (2004) speculated that the H_2O masers may arise in the accretion shock where gas is falling onto the central protostar. Maser emission, H_2O absorption, and CO absorption all paint a consistent picture of warm, dense gas very close to and falling toward, if not onto, the central source.

5.2. Comparison with Model Results

As previously stated, the relative abundance of H_2O with respect to H_2 in the warm gas in protostellar envelopes is expected to be 10^{-4} . The reason for this high water abundance is twofold. First, when the dust temperature is above about 100 K all of the water ice evaporates, drastically increasing the gas-phase H_2O abundance. Second, when the gas temperature is above about 300 K neutral-neutral reactions of H_2 with O and OH rapidly drive all of the remaining free oxygen into H_2O . Chemical models that account for changes in the physical structure of protostellar systems with time predict that as time progresses larger portions of the envelope will be at high temperature (Ceccarelli et al. 1996), thus increasing the total gas-phase water abundance and the ratio of gas-to-solid H_2O . This suggests the gas-to-solid water ratio as a potential tracer of protostellar evolution. Indeed,

Boonman & van Dishoeck (2003) find that larger H₂O abundances and larger gas-to-solid ratios correlate with higher temperatures, the presence of molecules that trace more evolved sources, and evidence of thermal processing in ices. Our water observations are consistent with the picture of AFGL 2136 IRS 1 as a more evolved protostar, and the increased water column density with respect to that reported by Boonman & van Dishoeck (2003) brings the gas-to-solid ratio into better agreement with what those authors found for AFGL 2591 and AFGL 4176, two other highly evolved sources.

It is also interesting to compare our results to physical models of protostellar envelopes. van der Tak et al. (2000) used dust emission and molecular line emission maps to infer density profiles of the form $n(r) = n_0(r/r_0)^{-\alpha}$ for several massive protostars. In the case of AFGL 2136 they found $r_0 = 35000$ AU, $n_0 = 3.6 \times 10^4$ cm⁻³, and $\alpha = 1.25$, with the model applicable for radii in the range $r_0/150 \leq r \leq 2r_0$. The density at the inner radius (233 AU) is about 2×10^7 cm⁻³, much smaller than the lower limit we infer, and a path length of greater than a few hundred AU is necessary to reach a column density comparable to that quoted above for warm H₂. However, they also found unresolved compact emission at 86 GHz indicative of a warm dust shell or circumstellar disk with radius $\lesssim 300$ AU. Such a region seems a favorable place to give rise to the water absorption features that we observe.

6. FUTURE PROSPECTS

The large water column density, $N(\text{H}_2\text{O}) \approx 10^{19}$ cm⁻², and warm temperature, $T \approx 500$ K, near AFGL 2136 IRS 1 combine to make absorption lines in the ν_1 and ν_3 bands observable. To determine the utility of such observations in other sources, we briefly examined predicted line strengths given different values of T and $N(\text{H}_2\text{O})$ assuming LTE. Given the noise level in our spectrum, at 400 K about 75% of the transitions we detected would still be observable, while at 300 K only about 25% would remain observable. Similarly, a reduction in the water column density to 10^{18} cm⁻² drops the number of detectable transitions to about 25% of those observed. It is no surprise then that our identical observations of Elias 29—where $N(\text{H}_2\text{O}) = (7 \pm 4) \times 10^{17}$ cm⁻²; $T = 350 \pm 200$ K (Boogert et al. 2000)—yield no detections of water lines in absorption. On the other hand, our initial observations of AFGL 4176 ($N(\text{H}_2\text{O}) = (1.5 \pm 0.7) \times 10^{18}$ cm⁻²; $T = 400 \pm 250$ K; Boonman & van Dishoeck 2003) do show water absorption near 2.5 μm (to be presented in a future publication). Clearly, there is a range of temperatures and water column densities over which these observations in the near-IR are currently feasible. The twelve massive protostars studied by Boonman & van Dishoeck (2003) represent a good sample of sources for initial consideration, with AFGL 2591, NGC 3576, and AFGL 2059 being particularly favorable targets

beyond the two already observed. As telescopes and detectors continue to improve the ν_1 and ν_3 bands of water should become useful tracers of physical conditions in a wide variety of star-forming regions.

7. SUMMARY

Our observations represent the first extensive study of water absorption in the near-infrared. Assigning absorption features to 47 separate transitions, we constructed a rotation diagram which is indicative of LTE for levels as high as 4294.5 K above ground. A statistical equilibrium analysis of all level populations gives best-fit parameters of $T = 506 \pm 25$ K, $n(\text{H}_2) > 5 \times 10^9 \text{ cm}^{-3}$, and $N(\text{H}_2\text{O}) = (1.02 \pm 0.02) \times 10^{19} \text{ cm}^{-2}$. These conditions are consistent with those inferred from observations of both CO in absorption and 22 GHz H_2O maser emission. Warm, very dense gas is in close proximity to AFGL 2136 IRS 1 and is likely falling toward, if not onto the massive protostar.

The authors thank the anonymous referee for suggestions to improve the clarity of the paper. N.I. and D.A.N. are funded by NASA Research Support Agreement No. 1393741 provided through JPL. M.J.R. is supported by NASA Collaborative Agreement NNX13ai85a.

REFERENCES

- Benson, P. J., & Little-Marenin, I. R. 1996, *ApJS*, 106, 579
- Boogert, A. C. A., Tielens, A. G. G. M., Ceccarelli, C., et al. 2000, *A&A*, 360, 683
- Boonman, A. M. S., & van Dishoeck, E. F. 2003, *A&A*, 403, 1003
- Brooke, T. Y., Sellgren, K., & Geballe, T. R. 1999, *ApJ*, 517, 883
- Carr, J. S., Tokunaga, A. T., & Najita, J. 2004, *ApJ*, 603, 213
- Ceccarelli, C., Hollenbach, D. J., & Tielens, A. G. G. M. 1996, *ApJ*, 471, 400
- Cernicharo, J., Thum, C., Hein, H., et al. 1990, *A&A*, 231, L15
- Cheung, A. C., Rank, D. M., Townes, C. H., Thornton, D. D., & Welch, W. J. 1969, *Nature*, 221, 626
- Daniel, F., Dubernet, M.-L., & Grosjean, A. 2011, *A&A*, 536, A76

- de Wit, W. J., Hoare, M. G., Oudmaijer, R. D., et al. 2011, *A&A*, 526, L5
- Doty, S. D., van Dishoeck, E. F., van der Tak, F. F. S., & Boonman, A. M. S. 2002, *A&A*, 389, 446
- Elitzur, M., Hollenbach, D. J., & McKee, C. F. 1989, *ApJ*, 346, 983
- Gerakines, P. A., Whittet, D. C. B., Ehrenfreund, P., et al. 1999, *ApJ*, 522, 357
- Gonzalez-Alfonso, E., Cernicharo, J., van Dishoeck, E. F., Wright, C. M., & Heras, A. 1998, *ApJ*, 502, L169
- Indriolo, N., Neufeld, D. A., Seifahrt, A., & Richter, M. J. 2013, *ApJ*, 764, 188
- Kastner, J. H., Weintraub, D. A., & Aspin, C. 1992, *ApJ*, 389, 357
- Kastner, J. H., Weintraub, D. A., Snell, R. L., et al. 1994, *ApJ*, 425, 695
- Käuff, H., Ballester, P., Biereichel, P., et al. 2004, *Proc. SPIE*, 5492, 1218
- Melnick, G. J., Menten, K. M., Phillips, T. G., & Hunter, T. 1993, *ApJ*, 416, L37
- Menten, K. M., Melnick, G. J., & Phillips, T. G. 1990a, *ApJ*, 350, L41
- Menten, K. M., Melnick, G. J., Phillips, T. G., & Neufeld, D. A. 1990b, *ApJ*, 363, L27
- Menten, K. M., & van der Tak, F. F. S. 2004, *A&A*, 414, 289
- Minchin, N. R., Hough, J. H., Burton, M. G., & Yamashita, T. 1991, *MNRAS*, 251, 522
- Mitchell, G. F., Maillard, J.-P., Allen, M., Beer, R., & Belcourt, K. 1990, *ApJS*, 363, 554
- Murakawa, K., Preibisch, T., Kraus, S., & Weigelt, G. 2008, *A&A*, 490, 673
- Najita, J. R., Edwards, S., Basri, G., & Carr, J. 2000, *Protostars and Planets IV*, 457
- Neufeld, D. A. 2010, *ApJ*, 708, 635
- Neufeld, D. A., Zmuidzinas, J., Schilke, P., & Phillips, T. G. 1997, *ApJ*, 488, L141
- Pontoppidan, K. M., Salyk, C., Blake, G. A., & Käuff, H. U. 2010a, *ApJ*, 722, L173
- Pontoppidan, K. M., Salyk, C., Blake, G. A., et al. 2010b, *ApJ*, 720, 887
- Salyk, C., Pontoppidan, K. M., Blake, G. A., et al. 2008, *ApJ*, 676, L49
- Seifahrt, A., Käuff, H. U., Zängl, G., et al. 2010, *A&A*, 524, A11

- Sheffer, Y., Rogers, M., Federman, S. R., Lambert, D. L., & Gredel, R. 2007, *ApJ*, 667, 1002
- Sonnentrucker, P., Neufeld, D. A., Phillips, T. G., et al. 2010, *A&A*, 521, L12
- Sunada, K., Nakazato, T., Ikeda, N., et al. 2007, *PASJ*, 59, 1185
- Valdettaro, R., Palla, F., Brand, J., et al. 2001, *A&A*, 368, 845
- van der Tak, F. F. S., van Dishoeck, E. F., Evans, II, N. J., & Blake, G. A. 2000, *ApJ*, 537, 283
- van Dishoeck, E. F., & Helmich, F. P. 1996, *A&A*, 315, L177
- van Dishoeck, E. F., Helmich, F. P., de Graauw, T., et al. 1996, *A&A*, 315, L349
- van Dishoeck, E. F., Kristensen, L. E., Benz, A. O., et al. 2011, *PASP*, 123, 138
- Willner, S. P., Gillett, F. C., Herter, T. L., et al. 1982, *ApJ*, 253, 174

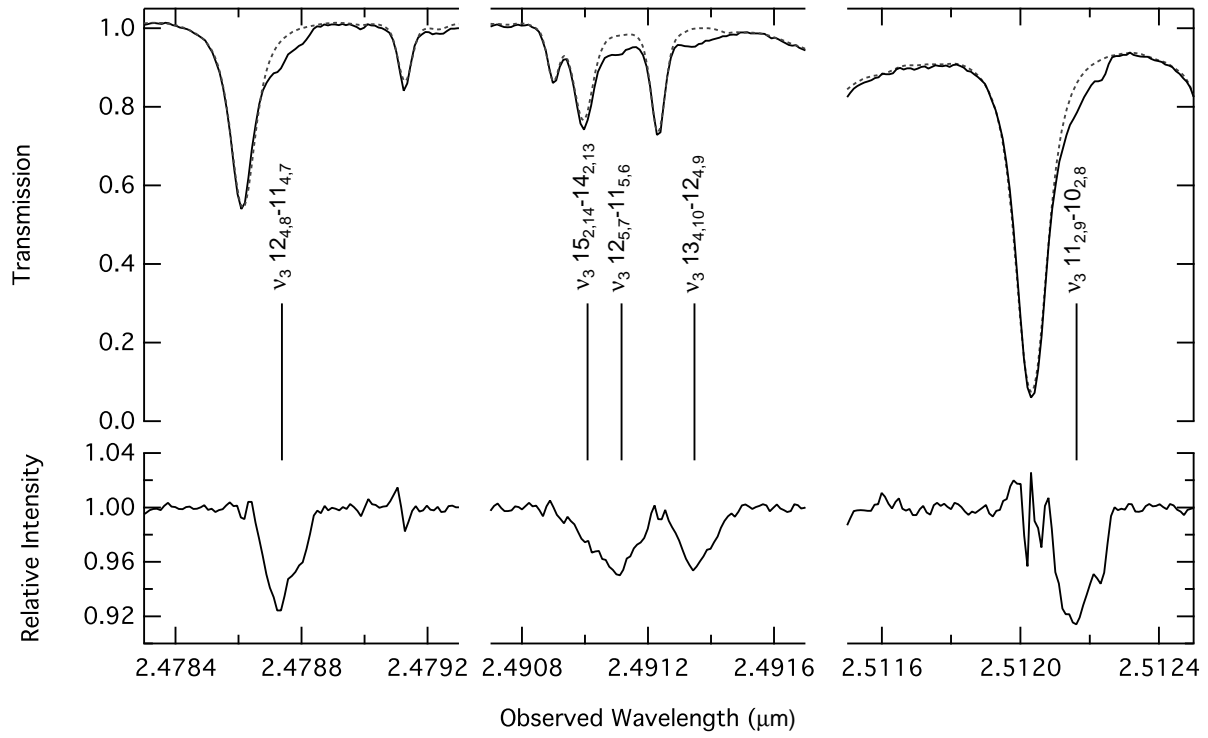


Fig. 1.— Select wavelength regions showing the observed spectra (solid) and model atmospheric spectra (dashed) above, and the observed divided by model spectra below. In all cases there is absorption at about $+15 \text{ km s}^{-1}$ (marked by vertical lines) with respect to the atmospheric water features.

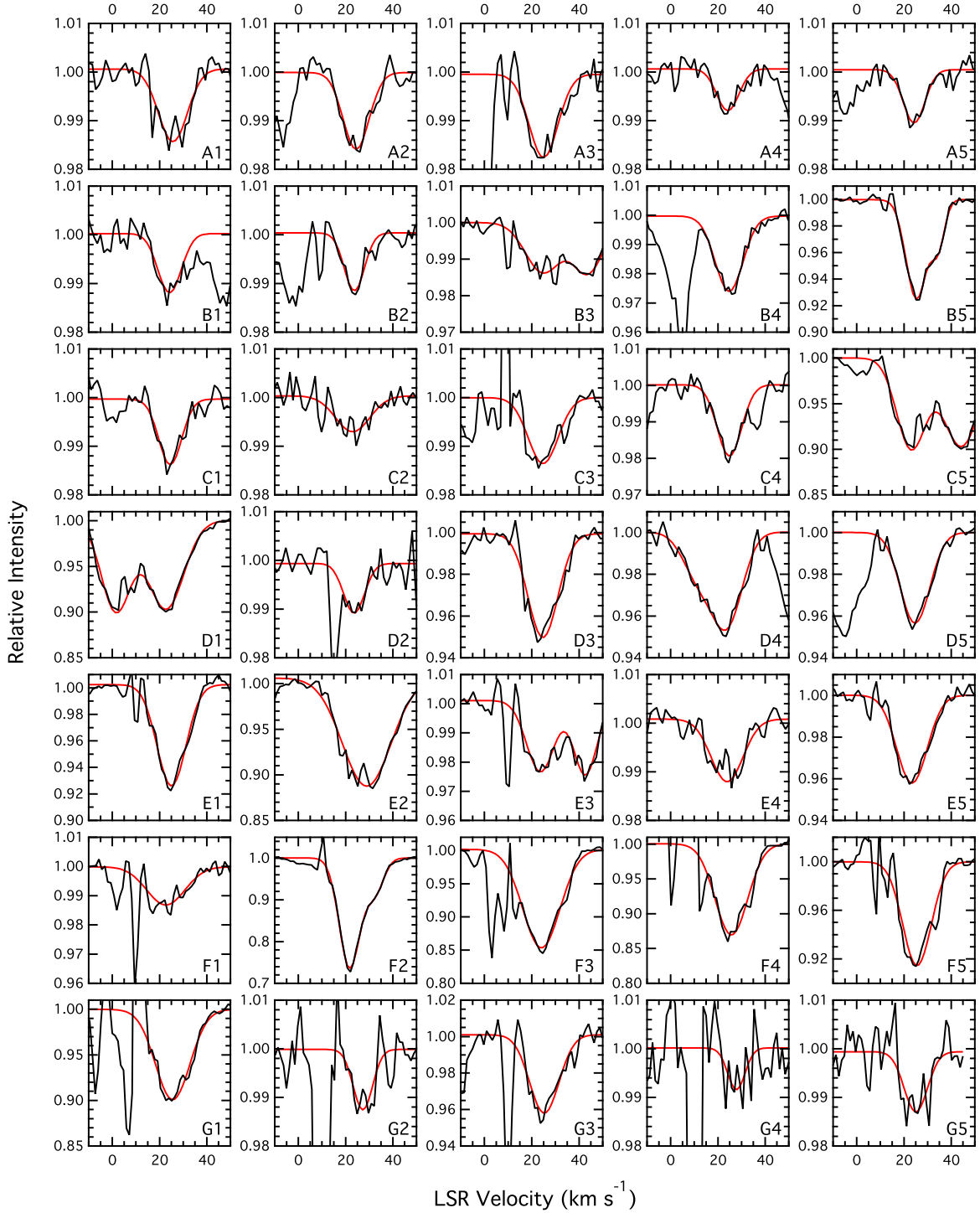


Fig. 2.— Spectra showing all 35 absorption features found in our analysis. Transition identifications for each panel are given in Table 1. Note the different relative intensity scales for each panel. In many cases, features near 10 km s⁻¹ are due to incomplete removal of telluric water lines.

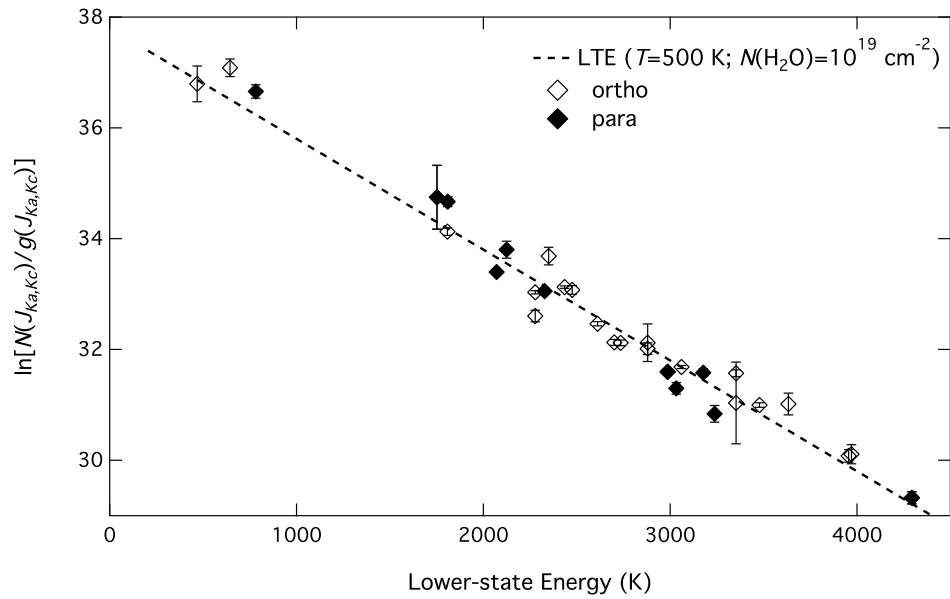


Fig. 3.— Rotation diagram for unblended transitions where column densities could be determined. Ortho levels are given by open diamonds, and para levels by filled diamonds. The dashed line is *not* a fit to the data, but marks the expected populations for LTE at $T = 500$ K with $N(\text{H}_2\text{O}) = 10^{19} \text{ cm}^{-2}$.

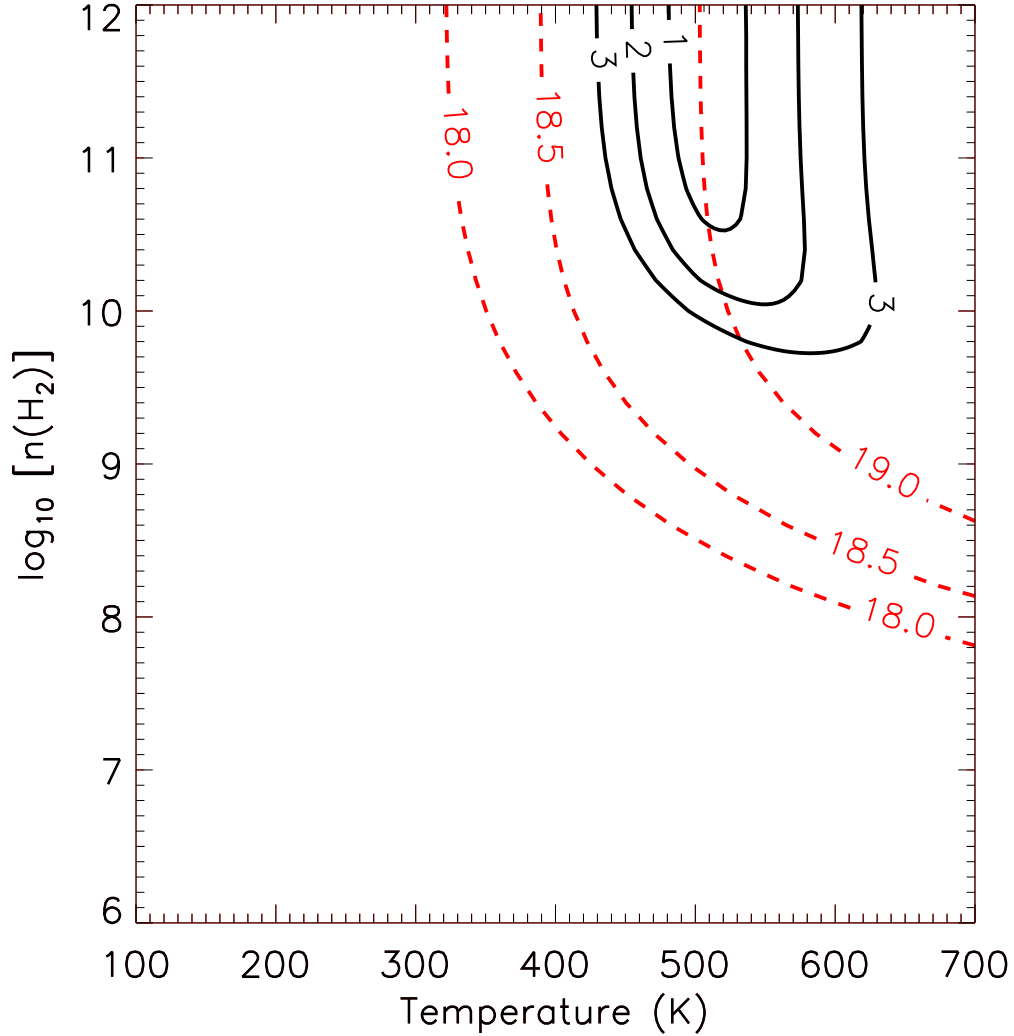


Fig. 4.— Best fit temperature, density, and H_2O column density as determined from a statistical equilibrium analysis of the level populations given in Table 1. Solid black contours show the quantity $(\chi^2 - N_{\text{dof}})^{1/2}$, where N_{dof} is the number of degrees of freedom (i.e., the number of independent data points minus the number of fitted parameters). These contours represent 68.3%, 95.4% and 99.7% confidence limits. Here, the χ^2 has been scaled (downward) to make its minimum value equal N_{dof} . The required reduction factor suggests that the statistical error estimates in Table 1 are smaller than the actual typical errors by a factor 4.29, a discrepancy that presumably reflects the presence of systematic errors. Dashed red contours show the values of $\log_{10}[N(\text{H}_2\text{O})/\text{cm}^{-2}]$ needed to fit the data. The statistical equilibrium analysis presented here includes the effects of radiative trapping of far-infrared water transitions for an assumed value of 10^{18} cm^{-2} per km s^{-1} for $N(\text{H}_2\text{O})/\Delta v$.

Table 1. Absorption Line Parameters

Wavelength (μm)	Transition	E/k (K)	W_λ -Pred. ($10^{-6} \mu\text{m}$)	W_λ -Obs. ($10^{-6} \mu\text{m}$)	$\sigma(W_\lambda)$ ($10^{-6} \mu\text{m}$)	v_{LSR} (km s^{-1})	FWHM (km s^{-1})	$N(J_{K_a, K_c})$ (10^{15}cm^{-2})	$\sigma(N)$ (10^{15}cm^{-2})	Figure 2 Panel	Comments
2.4686156	ν_1 12 _{6,7} -11 _{5,6}	2879.4	1.95	1.89	0.20	25.6	14.4	5.52	0.57	A1	...
2.4689113	ν_3 13 _{4,9} -12 _{4,8}	3177.1	1.57	1.79	0.12	24.5	13.0	1.30	0.09	A2	...
2.4732020	ν_1 11 _{6,5} -10 _{5,6}	2475.7	1.73	2.16	0.17	25.0	14.4	14.6	1.13	A3	...
2.4738368	ν_3 14 _{6,8} -13 _{6,7}	3970.4	0.65	0.84	0.15	24.2	11.1	0.96	0.17	A4	...
2.4740698	ν_3 18 _{1,18} -17 _{1,17}	4294.5	0.23	0.19 ^b	0.02 ^b	A5	blend 1
2.4740698	ν_3 18 _{0,18} -17 _{0,17}	4294.5	0.70	1.04 ^a	0.12 ^a	24.3	10.8	0.57 ^b	0.06 ^b	A5*	blend 1
2.4748404	ν_3 15 _{4,12} -14 _{4,11}	3955.5	1.04	1.25	0.14	24.2	11.7	1.01	0.11	B1	...
2.4752485	ν_1 11 _{5,6} -10 _{4,7}	2277.8	2.00	1.05	0.11	23.7	10.0	9.10	0.95	B2	...
2.4757180	ν_1 10 _{7,4} -9 _{6,3}	2349.9	1.18	2.11	0.34	24.8	17.6	24.3	3.87	B3	HF $R(1)$
2.4774810	ν_3 14 _{3,11} -13 _{3,10}	3478.3	2.70	3.14	0.13	24.7	13.9	2.35	0.09	B4	...
2.4785984	ν_3 12 _{4,8} -11 _{4,7}	2735.4	10.8	8.75 ^c	0.46 ^c	6.15	0.32	B5	...
2.4833761	ν_3 13 _{3,10} -12 _{3,9}	3033.4	2.11	1.36	0.14	24.5	11.5	0.98	0.10	C1	...
2.4861802	ν_1 10 _{6,4} -9 _{5,5}	2124.6	0.87	1.11	0.17	23.0	17.1	9.10	1.39	C2	...
2.4868917	ν_1 7 _{4,4} -6 _{1,5}	782.0	1.17	1.78	0.22	24.8	14.9	108	13.2	C3	...
2.4887954	ν_2 15 _{3,12} -14 _{2,13}	3353.2	1.31	2.10	0.13	24.9	12.2	4.47	0.28	C4	...
2.4893977	ν_3 12 _{3,9} -11 _{3,8}	2611.8	14.3	12.7	0.49	23.1	14.5	8.66	0.34	C5	...
2.4895351	ν_3 14 _{2,12} -13 _{2,11}	3236.5	4.64	< 10.7	...	D1	blend 2
2.4895765	ν_3 16 _{0,16} -15 _{0,15}	3397.0	4.13	15.2 ^a	0.55 ^a	< 10.0	...	D1*	blend 2
2.4895766	ν_3 16 _{1,16} -15 _{1,15}	3397.0	1.38	< 10.0	...	D1	blend 2
2.4895769	ν_3 13 _{5,9} -12 _{5,8}	3277.5	3.09	< 13.7	...	D1	blend 2
2.4901296	ν_3 14 _{3,12} -13 _{3,11}	3238.2	1.54	0.95	0.14	23.6	10.5	0.67	0.10	D2	...
2.4904204	ν_3 11 _{4,7} -10 _{4,6}	2328.4	7.19	6.56	0.39	24.7	14.9	4.75	0.28	D3	...
2.4908999	ν_3 15 _{2,14} -14 _{2,13}	3353.2	2.87	2.70	2.00	23.4	15.2	2.61	1.93	D4	blend 3
2.4909997	ν_3 12 _{5,7} -11 _{5,6}	2879.4	5.41	5.85	1.98	23.9	15.2	6.16	2.08	D4*	blend 3
2.4912320	ν_3 13 _{4,10} -12 _{4,9}	3060.9	5.70	5.72	0.16	24.7	14.8	4.32	0.12	D5	...
2.4977585	ν_3 15 _{0,15} -14 _{0,14}	2986.8	3.08	1.53 ^b	0.07 ^b	E1	blend 4
2.4977590	ν_3 15 _{1,15} -14 _{1,14}	2986.8	9.22	9.74 ^a	0.43 ^a	25.0	14.4	4.59 ^b	0.20 ^b	E1*	blend 4
2.4981464	ν_3 13 _{3,11} -12 _{3,10}	2826.9	10.2	25.4 ^a	1.24 ^a	< 17.2	...	E2*	blend 5
2.4982130	ν_3 14 _{1,13} -13 _{1,12}	2941.8	9.06	< 16.5	...	E2	blend 5
2.4982710	ν_3 14 _{2,13} -13 _{2,12}	2941.9	3.02	< 16.5	...	E2	blend 5
2.4991990	ν_1 9 _{6,3} -8 _{5,4}	1808.0	3.18	3.00	0.20	23.7	13.4	33.8	2.30	E3	HF $R(0)$
2.4997063	ν_1 9 _{6,4} -8 _{5,3}	1809.1	1.12	1.82	0.16	23.9	15.9	19.3	1.74	E4	...
2.5006937	ν_3 12 _{5,8} -11 _{5,7}	2860.4	2.22	< 5.05	...	E5	blend 6
2.5007295	ν_3 12 _{4,9} -11 _{4,8}	2654.8	4.01	5.70 ^a	0.19 ^a	< 4.22	...	E5*	blend 6

Table 1—Continued

Wavelength (μm)	Transition	E/k (K)	W_λ -Pred. ($10^{-6} \mu\text{m}$)	W_λ -Obs. ($10^{-6} \mu\text{m}$)	$\sigma(W_\lambda)$ ($10^{-6} \mu\text{m}$)	v_{LSR} (km s^{-1})	FWHM (km s^{-1})	$N(J_{K_a, K_c})$ (10^{15}cm^{-2})	$\sigma(N)$ (10^{15}cm^{-2})	Figure 2 Panel	Comments
2.5018269	ν_1 8 _{7,1} -7 _{6,2}	1751.8	0.35	18.5 ^b	10.6 ^b	F1	blend 7
2.5018296	ν_1 8 _{7,2} -7 _{6,1}	1751.8	1.06	2.21 ^a	1.27 ^a	22.7	19.0	55.5 ^b	31.9 ^b	F1*	blend 7
2.5045908	ν_3 12 _{2,10} -11 _{2,9}	2435.3	21.8	30.8 ^c	0.68 ^c	16.8	0.38	F2	...
2.5066038	ν_3 12 _{3,10} -11 _{3,9}	2441.6	6.98	< 15.8	...	F3	blend 8
2.5066091	ν_3 13 _{2,12} -12 _{2,11}	2556.4	19.0	24.3 ^a	0.37 ^a	< 15.1	...	F3*	blend 8
2.5112606	ν_3 11 _{4,8} -10 _{4,7}	2277.8	23.6	19.0	0.56	25.7	16.2	14.0	0.41	F4	...
2.5120359	ν_3 11 _{2,9} -10 _{2,8}	2071.3	14.0	10.8	0.50	25.5	14.2	6.71	0.31	F5	...
2.5126941	ν_1 8 _{6,3} -7 _{5,2}	1526.6	3.10	< 273	...	G1	blend 9
2.5127076	ν_3 11 _{5,7} -10 _{5,6}	2475.7	13.4	15.2 ^a	0.44 ^a	< 13.2	...	G1*	blend 9
2.5133118	ν_1 7 _{2,5} -6 _{1,6}	644.2	0.61	1.07	0.17	27.3	9.6	497	78.6	G2	...
2.5184602	ν_3 11 _{6,6} -10 _{6,5}	2700.8	7.38	5.61	0.30	25.3	14.6	5.64	0.30	G3	...
2.5204395	ν_1 6 _{3,4} -5 _{0,5}	468.6	0.70	0.65	0.21	27.8	8.6	315	102	G4	...
2.5209404	ν_3 12 _{8,4} -11 _{8,3}	3633.2	0.80	1.29	0.25	25.0	11.6	2.04	0.40	G5	...

Note. — Columns 1, 2, and 3 give the transition wavelength, label, and lower state energy. Column 4 is the predicted equivalent width, W_λ -Pred, assuming a total water column density of 10^{19}cm^{-2} in LTE at 500 K. Columns 5 and 6 are the observed equivalent width, W_λ -Obs, and its 1σ statistical uncertainty returned by the fitting procedure. Systematic uncertainties—due to, e.g., working around poorly removed atmospheric features and setting the continuum level—may be somewhat larger. Columns 7 and 8 are the line-center velocity and velocity full-width at half-maximum (including instrumental broadening effects) found by a Gaussian fit to the absorption feature. In cases where blended lines were fit with a single Gaussian component or where features with shoulders were fit with two Gaussian components, velocity information is not reported. Columns 9 and 10 are the column density in the lower state, N , and its 1σ uncertainty. Upper limits on column densities are calculated assuming the entire equivalent width of a blended feature is due only to each contributing line in turn. Column 11 gives the panel in Figure 2 in which the absorption feature is shown. For blended lines, an asterisk next to the panel label denotes the transition wavelength used to set zero velocity on the bottom axis. Note that beyond the 47 detected transitions that are tabulated above we predict an additional 42 transitions covered by our observations that should be above the detection limit of $W_\lambda > 6 \times 10^{-7} \mu\text{m}$ assuming LTE at 500 K and $N(\text{H}_2\text{O}) = 10^{19} \text{cm}^{-2}$. All of these transitions are either obscured by strong telluric lines (39) or affected by bad pixels on the detector (3). Non-detections are consistent with predicted equivalent widths, and in no case is a transition that we expect to see “missing”.

^aTotal equivalent width of absorption feature containing multiple blended lines.

^bColumn densities and uncertainties were calculated using the equivalent width of the blended feature and assuming an ortho-to-para ratio of 3:1.

^cSum of 2 components used to fit absorption features with shoulders.